Near-liquidus growth of feldspar spherulites in trachytic melts: 3D morphologies and implications in crystallization mechanisms

Fabio Arzilli [a,*], Lucia Mancini [a], Marco Voltolini [b], Maria Rita Cicconi [c], Sara Mohammadi [a,d], Gabriele Giuli [c], David Mainprice [e], Eleonora Paris [c], Fabrice Barou [e], Michael R. Carroll [c]

[a] Elettra-Sincrotrone Trieste S.C.p.A., SS 14, Km 163.5 in Area Science Park, 34149 Basovizza, Trieste, Italy
[b] Lawrence Berkeley National Laboratory, 1 Cyclotron Rd, 94720 Berkeley, CA, USA
[c] School of Science and Technology — Geology Division, University of Camerino, Via Gentile III da Varano, 62032 Camerino, Italy
[d] The "Abdus Salam" International Centre for Theoretical Physics (UNESCO), Strada Costiera 11, 34151 Trieste, Italy
[e] Geosciences Montpellier UMR CNRS 5243, Université Montpellier 2, 34095 Montpellier Cedex 05, France

ABSTRACT

The nucleation and growth processes of spherulitic alkali feldspar have been investigated in this study through X-ray microtomography and electron backscatter diffraction (EBSD) data. Here we present the first data on Shape Preferred Orientation (SPO) and Crystal Preferred Orientation (CPO) of alkali feldspar within spherulites. The analysis of synchrotron X-ray microtomography and EBSD datasets allowed us to study the morphometric characteristics of spherulites in trachytic melts in quantitative fashion, highlighting the three-dimensional shape, preferred orientation, branching of lamellae and crystal twinning, providing insights about the nucleation mechanism involved in the crystallization of the spherulites. The nucleation starts with a heterogeneous nucleus (pre-existing crystal or bubble) and subsequently it evolves forming "bow tie" morphologies, reaching radially spherulitic shapes in few hours. Since each lamella within spherulite is also twinned, these synthetic spherulites cannot be considered as single nuclei but crystal aggregates originated by heterogeneous nucleation. A twin boundary may have a lower energy than general crystal–crystal boundaries and many of the twinned grains show evidence of strong local bending which, combined with twin plane, creates local sites for heterogeneous nucleation.

This study shows that the growth rates of the lamellae (10^{-6}–10^{-7} cm/s) in spherulites are either similar or slightly higher than that for single crystals by up to one order of magnitude. Furthermore, the highest volumetric growth rates (10^{-11}–10^{-12} cm^3/s) show that the alkali feldspar within spherulites can grow fast reaching a volumetric size of ~10 μm^3 in 1 s.

© 2014 Elsevier B.V. All rights reserved.

1. Introduction

Spherulites are confocal radial polycrystalline aggregates that commonly occur in a wide variety of materials crystallized under highly non-equilibrium conditions (Gránásy et al., 2005; Watkins et al., 2009). In geology, spherulitic textures observed in volcanic rocks (Baker and Freda, 2001; Breitkreuz, 2013; Castro et al., 2008; Clay et al., 2012; Keith and Padden, 1963; Lofgren, 1971a; Monecke et al., 2004; Seaman, 2013; Smith et al., 2001; Watkins et al., 2009), typically consist of radiating structure that can be formed by alkali feldspar, plagioclase, cristobalite and pyroxene (Lofgren, 1971a). Polymineralic spherulitic aggregates, such as intergrowths of quartz, feldspar and magnetite (Castro et al., 2008; Seaman, 2013), or feldspar, pyroxene and biotite (Kesler and Weiblen, 1968) are quite common in silicate melts. The formation conditions of spherulitic textures in natural silicate materials are still much debated, with some studies suggesting subsolidus formation (Lofgren, 1971a) and others suggesting formation from strongly undercooled liquids (Fenn, 1977; Swanson, 1977).

Understanding the growth of spherulites as a function of temperature (T), undercooling ($\Delta T = T_{liquidus} - T_{experimental}$), pressure ($P_{H_2O}$) and superheating ($-\Delta T = T_{above\ liquidus} - T_{liquidus}$) is critical to investigations of the physical–chemical conditions required for spherulite growth. Previous studies have shown that spherulitic shapes are strongly dependent on ΔT and cooling rate (Fenn, 1977; Lofgren, 1974). Spherulitic growth as a function of cooling could include a primary crystallization at high undercooling ($\Delta T > 200$ °C), resulting in a rapid crystallization above the glass transition temperature (T_g) (Baker and Freda, 2001; Castro et al., 2008; Clay et al., 2012; Dunbar et al., 1995; Fenn, 1977; Monecke et al., 2004; Smith et al., 2001; Swanson, 1977), or hydration and devitrification below T_g (Castro et al., 2008; Lofgren, 1971a,b; Stasiuk et al., 1996; Swanson et al., 1989; Watkins et al., 2009).

To study the crystallization of spherulitic alkali feldspar in trachytic melts a dual approach was employed. The first one was to study

three-dimensional features of spherulitic textures from a previous experimental study (Arzilli and Carroll, 2013) in order to obtain information about their shapes, morphologies of lamellae and the nucleation mechanisms. The second one was to obtain the Crystal Preferred Orientation (CPO) through electron backscatter diffraction (EBSD) technique. The latter approach employs EBSD analysis to examine the incipient stages of alkali feldspar crystallization within spherulites. The complementary nature of a technique able to provide 3D morphometric information (synchrotron X-ray computed microtomography) with a technique focused at getting crystallographical information (EBSD) through 2D images, allowed us to obtain crucial information on the nucleation mechanism (homogeneous vs heterogeneous) at the scale of 1 μm and its influence on the growth and twinning.

3D textural analysis is a powerful tool to derive crystal shapes and preferred orientations based on the morphology of the objects: a Shape Preferred Orientation (SPO). Depending on the relationship between shape and crystallographic orientation SPO and CPO might or might not be related, and the two approaches for texture analysis are complementary (Zucali et al., 2014). In this work a novel approach for the microtomographic data analysis has been employed: the synchrotron X-ray microtomography data were collected taking advantage of the coherence of synchrotron X-rays to obtain a phase contrast effect (in "near field" conditions) due to free space propagation to highlight the interfaces between feldspars and glass. This effect provides an edge enhancement that aids the visualization, compared to more "pure absorption" experimental setups (Baker et al., 2012). On the other hand, phase-contrast artifacts are a significant problem when trying to obtain volumes with binary data that commonly are the starting point for morphometric analysis. The density contrast between feldspars and glass is too weak to provide a good separation of the two materials. Single distance phase-retrieval algorithms can be employed on this kind of dataset to obtain two main results: i) the effect of the phase-contrast artifacts is canceled (in ideal cases) or at least reduced; and ii) the phase information retrieved provides a better contrast in the reconstructed images. The consequence of this processing is generally a slight blurring of images, since acquiring conditions can be quite far from the ideal ones (~homogeneous monophase "phase objects" and perfectly monochromatic X-ray beam). These algorithms can be employed, with some caution, even on dense materials and with polychromatic light (e.g., Meyers et al., 2007). Our results show for the first time the application of such algorithms on rocks in a case where the application is crucial in providing a segmentable dataset for quantitative analysis.

2. Material and methods

2.1. Sample preparation and experimental conditions

The data on spherulites were extracted from results of the experimental study of Arzilli and Carroll (2013). Dynamic crystallization experiments, performed by Arzilli and Carroll (2013), were used to study the crystallization of alkali feldspar spherulites. In detail, cooling, isothermal decompression and "cooling + decompression" experiments were performed by Arzilli and Carroll (2013) to investigate crystallization kinetics of alkali feldspar in trachytic melts. During cooling experiments, initial conditions of P–T were maintained above the sanidine liquidus for 2–3 h for all experiments. Investigated pressures ranged from 200 to 50 MPa; pressure was constant during the run, while temperature was quickly decreased from initial (880 and 900 °C) to final T (ranging between 750 and 855 °C), then final conditions were maintained for variable times (2, 4, 6, 8, 14 and 16 h) in order to study the effect of time on crystallization (Arzilli and Carroll, 2013). A similar approach was used for isothermal decompression experiments but the temperature was constant (800, 825 and 840 °C) and the pressure was decreased from initial (200 and 150 MPa) to final P (100, 70, 50 and 30 MPa) (Arzilli and Carroll, 2013). During

"cooling + decompression" experiments the initial pressure (200, 150 and 100 MPa) and the initial temperature (850 °C) were held above the sanidine liquidus for 2 or 3 h. Then temperature was decreased to 750 °C (final temperature, T_f) and the pressure was lowered to the run value (P_f: 150, 100, 50, 30 MPa) (Arzilli and Carroll, 2013). Due to the negative slope of the alkali feldspar liquidus in P_{H_2O}–T space, several ΔT and −ΔT were investigated by Arzilli and Carroll (2013) during the experiments (see Supplementary Table 1). Complete procedure of sample preparation and experimental details are reported in Arzilli and Carroll (2013).

All experimental samples were analyzed by scanning electron microscopy in order to investigate all phases present. On the basis of textural features, 12 samples were analyzed using phase-contrast synchrotron X-ray computed microtomography and the two most representative samples (D85 and D1) were chosen to study the 3D shapes and orientations of lamellae in spherulites. Samples D85 and D1 were obtained through cooling experiments (Arzilli and Carroll, 2013) and they were characterized by experimental durations of 6 and 4 h respectively. These durations allowed us to analyze a sufficient number of spherulites to make statistical calculations of preferred orientations. Furthermore, spherulites were characterized by widely spaced crystals so lamellae were more easily separable from the glass than those obtained in 14 h. The analyzed volumes of D85 and D1 were 12.1 mm³ and 3.95 mm³ respectively.

2.2. Analytical methods

2.2.1. Phase-contrast synchrotron X-ray computed Microtomography (PC mCT)

White-beam phase-contrast synchrotron X-ray mCT (Baker et al., 2012) measurements were performed at the SYRMEP beamline of the Elettra-Sincrotrone Trieste in Basovizza (Trieste, Italy). The source of the SYRMEP beamline is a bending magnet and provides, at a distance of about 15 m from the source, a nearly parallel, laminar-section X-ray beam with a maximum area of 100 mm (horizontal) × 4 mm (vertical). The sample-to-detector distance was set at 150 mm. The detector used was an air-cooled, 16 bit, CCD camera (Photonic Science Ltd.) with a 2048 × 2048 pixel chip (KAI 4022 M CCD). The optical system is based on the indirect detection of X-rays using a scintillator screen coupled via visible light microscope optics to the CCD camera. A 100 μm thick, stand alone, single crystal LuAG:Ce (Ce doped lutetium–aluminum garnet $Lu_3Al_5O_{12}$) scintillator screen produced by Crytur (Czech Republic) was employed. The effective pixel size of the detector was set at 2.0 μm × 2.0 μm, thus yielding a maximum field of view of about 4.0 mm × 4.0 mm. For each sample 1800 radiographic images (or projections) were acquired by the detector with equi-angular steps over a range of 180° and an exposure time/projection of 3.2 s. The custom-developed software named *Syrmep_tomo_project* 4.0 and the Filtered Back-Projection (FBP) algorithm (Herman, 1980) were used to reconstruct the axial slices from the sample projections. These slices were then stacked to obtain volumes with an isotropic voxel size of 2.0 μm. The 3D visualization of the reconstructed volumes was obtained using the commercial software VGStudio MAX 2.0 (Volume Graphics).

2.2.2. Phase-retrieval processing

The biggest challenge in the image analysis of many volcanic rocks is the separation of the different phases to obtain the binarized volumes, since the absorption contrast of the crystals is often close to that of the glass. In some cases masking procedures can be used to separate the two phases (e.g., Zandomeneghi et al., 2010) using an approach based on shapes, but it is not applicable in the present case. Phase-contrast X-ray imaging provides images with contributions of absorption and refraction together. To enhance the contrast between different phases inside the sample (see Figs. 1, 2) and also to improve the reliability of quantitative morphological analysis, it is necessary to retrieve the phase distribution of the sample. For this objective, a single-distance
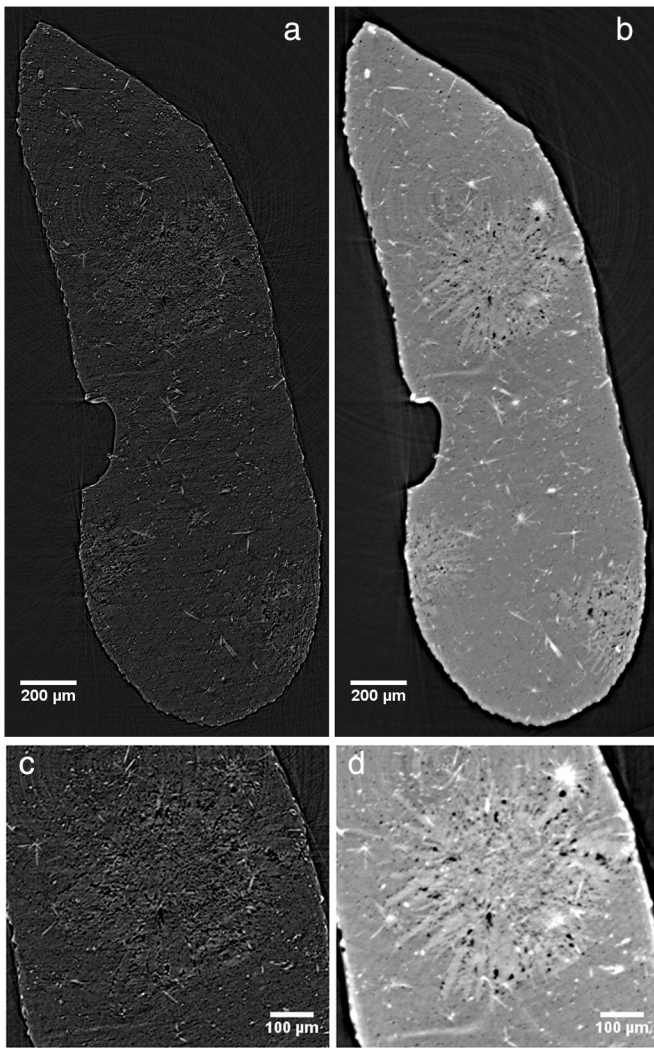
Fig. 1. Sample D1: Reconstructed axial slice before (a) and after (b) the phase-retrieval processing. The image in (b) shows spherulites of alkali feldspar (light gray), trachytic glass (dark gray), bubbles (black), clinopyroxenes and oxides (white). (c) Detailed image of the reconstructed axial slice shown in (a). (d) Detailed image of the slice shown in (b).

orientations. Since spherulite nucleus was either a crystal(s) or a bubble(s), the segmentation of the central crystal was complicated because it was quite difficult to see its real shape, due to the low contrast. The Shape Preferred Orientation (SPO) analysis has been carried out on single lamella using the procedure described in Voltolini et al. (2011). Moreover, the whole dataset of D1 (with 692 lamellae) was used to calculate the shape Orientation Distribution Function (ODF).

2.2.4. Electron backscatter diffraction (EBSD) measurements

Oriented polished surfaces were prepared from the recovered experimental specimens D85 and D1 surfaces previously used for traditional SEM observations, except for one powder particle that was mounted in epoxy resin and then polished. The EBSD analyses were obtained with a CamScan X500FE CrystalProbe equipped with an EBSD system at Geosciences Montpellier (France). The operating conditions were 15 kV, 3.5 nA, and a working distance of 25 mm under low vacuum conditions (5 Pa of gaseous nitrogen) to avoid electrical charging of the insulating experimental samples.

Texture analysis was performed using the EBSD technique. EBSD requires high integrity of the analyzed surface layers. A final polishing with colloidal silica suspension was performed to remove the damage in near surface layers introduced by mechanical grinding and polishing. The samples were not carbon-coated. The incoming electron beam is at an angle of 20° to the horizontal sample surface. Interaction of the electrons with a small volume of the sample (several nm^3) produces a diffraction pattern that reflects the crystal symmetry and orientation very near the sample surface. This pattern is projected onto a phosphor screen and recorded by a digital CCD camera. The image is then processed and indexed in terms of crystal orientation using the AZtec 2.0 software from Oxford Instruments HKL. For each sample using a combination of electron beam scan map and motorized specimen stage control, we obtained large-area crystallographic orientation maps covering almost the entire surface of the experimental samples. Sampling step sizes were 1.00 μm, 0.70 μm and 0.25 μm for 3 EBSD maps made on sample D85 as part of a preliminary study of spherulites.

Data treatment allowed increasing the percentage of indexed points (i) filling the non-indexed pixels that have up to 8 identical neighbors with this orientation and (ii) repeating this operation using, respectively, 7 and 6 identical neighbors. It also allowed us to identify the grains (i.e., continuous domains characterized by an internal misorientation less than 10°). At each step, the resulting orientation maps were verified to avoid over-extrapolation of the data. Crystallographic texture analysis was performed using MTEX (Bachmann et al., 2010, 2011; Hielscher and Schaeben, 2008; Mainprice et al., 2011, 2014a,b) a free and open source MATLAB® toolbox (https://github.com/mtex-toolbox/mtex). Two types of EBSD map were constructed using MTEX: an orientation map, where the color of each grain corresponds to its mean crystallographic orientation; and misorientation map, where the color at each orientation within the grain corresponds to the angle between the mean orientation of the grain and the orientation at that position. The Crystal Preferred Orientation (CPO) was observed using pole figures in the specimen reference frame, where X and Y define the specimen surface and Z is normal to the surface. Misorientation was examined using histograms of the minimum symmetrically equivalent rotation angle, also called disorientation, and the associated rotation axes in crystal coordinates. Finally, the crystal long-axis of each grain in the XY specimen plane was calculated using a specially developed MTEX script and the distribution illustrated as contoured diagrams in crystal coordinates for specific axial ratios.

2.3. Growth rate measurements

In this study, we estimated the growth rate of alkali feldspars in spherulites in order to quantify the growth kinetics of such morphologies. X-ray microtomography technique allowed us to obtain the 3D shape of spherulites for sample D1 and D85. Furthermore, the common
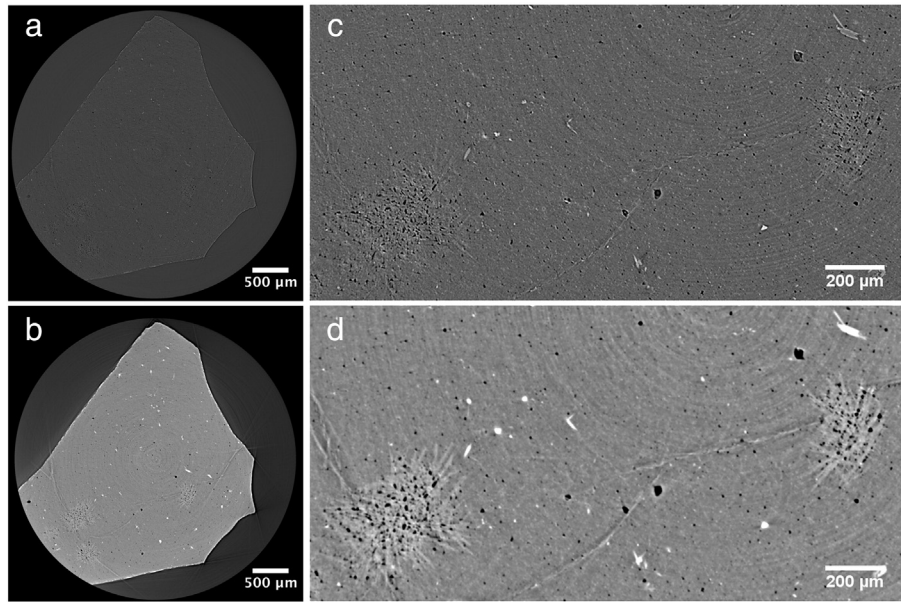
phase-retrieval algorithm was applied to the acquired dataset in order to separate crystals from silicate glass. This algorithm is based on Transport of Intensity Equation (TIE) (Paganin et al., 2002) and it is implemented in the X-TRACT software package developed by the CSIRO group (X-TRACT version 5.8) (X-TRACT, 2013). Phase-retrieval using the TIE algorithm, in combination with the FBP algorithm for tomographic reconstruction, allows us to obtain the 3D distribution of the complex refraction index, $n = 1 - \delta + i\beta$, of the material under consideration, where δ is the refractive index decrement and β is the absorption index. In this method, we utilize a priori known information about the sample which is characterized by a fixed proportionality relationship between the real and imaginary parts of the refractive index, $\delta / \beta = \gamma = $ constant (where the real and imaginary parts are related to phase and absorption distribution of the sample, respectively). For all of our samples we used $\gamma = 50$, the choice of this value allowed us to enhance he contrast between alkali feldspar and trachytic glass.

2.2.3. Image segmentation and preferred orientation analysis

The semi-automatic volume segmentation with manual corrections was carried out by means of AMIRA® software v.4.1.2 (Mercury Computer Systems) to separate the single lamellae grown within the spherulites, with the aim to study the shape of these crystals and their

Fig. 2. Sample D85: Reconstructed axial slice before (a) and after (b) the phase-retrieval processing. The image in (b) shows spherulites of alkali feldspar (light gray), trachytic glass (dark gray), bubbles (black), clinopyroxenes and oxides (white). (c) Detailed image of the axial slice shown in (a). (d) Detailed image of the slice shown in (b).

2D approach, already applied by several previous authors (e.g., Couch, 2003; Arzilli and Carroll, 2013), was used to compare the growth rates between spherulite and single alkali feldspar crystal (the latter estimated by Arzilli and Carroll, 2013).

2D crystal length (L_{2D}) of alkali feldspars within spherulites was measured using ImageJ software, which allows us to define the scale in pixel/μm. Hence, pixels were counted to obtain scaled length. The growth rates (Y_{L2D}) of the crystals in spherulites were estimated taking into account, for each sample, the 10 largest lamellae into the spherulite. The maximum growth rate was calculated using the relationship:

$$Y_{L2D} = L_{2D}/t_{exp}$$

where t_{exp} is the experimental duration.

By measuring 3D shape of alkali feldspar the real maximum axis length (L_{3D}) was obtained, therefore we were able to calculate the growth rate (Y_{L3D}) in samples D1 and D85. To make a comparison with Y_{L2D}, the 10 longest alkali feldspars in spherulites were measured for both samples. The maximum growth was estimated from:

$$Y_{L3D} = L_{3D}/t_{exp}.$$

The microtomography images give us the opportunity to measure the volume of crystals. Being able to obtain the 3D shape of feldspars within spherulites and knowing the duration of growth (experimental duration), we were able to calculate the growth rate in volumetric terms. The volumetric growth rate (Y_V) was calculated using the following relationship:

$$Y_V = (V * 0.5)/t_{exp}$$

where V is the volume of the crystal.

3. Results and discussion

3.1. Conditions of growth

In order to discuss the growth conditions of spherulites we show the results of Arzilli and Carroll (2013) about the appearance of these morphologies. The results of cooling, "decompression + cooling" and isothermal decompression experiments performed by Arzilli and Carroll

(2013) show that spherulites were present at: i) high pressures between 70 and 200 MPa (except D81 at 50 MPa) (Fig. 3), associated with water contents between ~3 and 7 wt.% in the melt; ii) low to medium ΔT between ~15 and 70 °C (Fig. 3); and iii) following large superheating between ~60 and 130 °C (Fig. 3). Spherulites crystallized in almost the whole range of investigated temperatures (750–840 °C), suggesting that the crystallization temperature does not have major importance for the development of such morphologies. However, temperature is an important variable in the growth process of spherulites, and the formation conditions are sensitive to pressure because liquidus temperatures and melt water contents are intimately linked to P_{H_2O}, which in turn controls the degree of undercooling and superheating of individual experimental samples at a given temperature.

The investigated undercooling from Arzilli and Carroll (2013) ranges between 2 and 140 °C and their results show that the combination of high superheating and low/intermediate undercooling permits
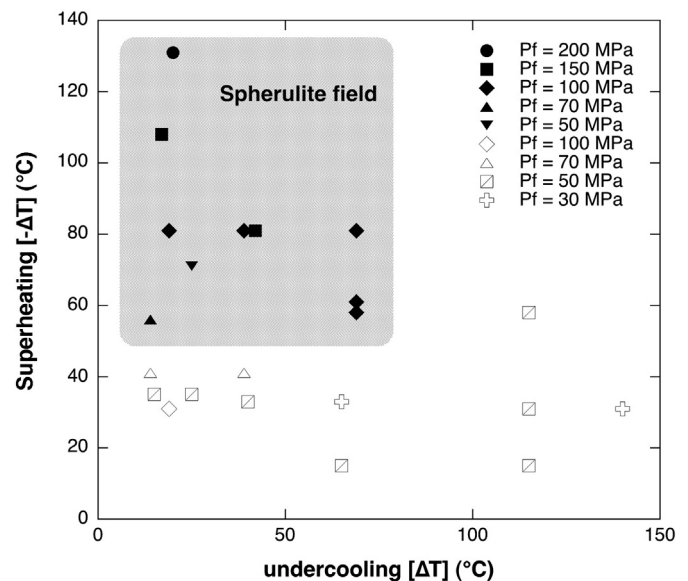

Fig. 3. Spherulite conditions of formation. Filled symbols show the experimental conditions where spherulites were grown, whereas the open symbols show experiments without spherulites. ($P_f = P_{H_2O}$ = final pressure of the experiment — all H_2O saturated).

crystallization of spherulites. The number and size of spherulites increase with increasing ΔT, until ΔT = 100 °C. For higher undercoolings, heterogeneous nucleation is dominant and samples are characterized by high crystal number density and crystal fraction, generating intensely crystallized samples without spherulitic textures (Arzilli and Carroll, 2013). Considering the first 100 °C of undercooling, the effect of ΔT is similar to that of time, since they act concurrently on crystallization processes, favoring the nucleation and growth of spherulites.

Results of Arzilli and Carroll (2013) show also that the development of spherulites is favored by rapid decompression and cooling, in agreement with previous studies (Dunbar et al., 1995; Fenn, 1977; Lofgren, 1974; Seaman, 2013; Swanson, 1977), and slow rates of cooling and decompression do not produce such morphologies (Brugger and Hammer, 2010; Conte et al., 2006).

3.2. Spherulitic shapes: nucleation and growth mechanism

We characterized the 3D structure of experimentally grown spherulites via phase-contrast synchrotron X-ray computed microtomography (PC mCT) of samples D85 and D1 (Figs. 4, 5) in order to better understand the nucleation mechanism. Crystals in spherulites are in contact with each other and we separated them to measure the shape Orientation Distribution Function (ODF).

To better understand the nucleation mechanism of such morphologies we applied a procedure aimed at SPO analysis (Voltolini et al., 2011) to the PC mCT datasets. As a first step, the projections were treated using a single-distance phase-retrieval algorithm (Paganin et al., 2002). This step was necessary because of the small difference in the absorption contrast (Cloetens et al., 1996) of feldspars and trachytic glass (see Figs. 1, 2). A semi-automatic volume segmentation procedure with manual corrections was applied to separate the single lamellae. The SPO analysis was carried out, using single lamellae, on the PC mCT datasets (Figs. 4, 5). Concerning D85, all spherulites present in the imaged volume were separated (8 individual spherulites) and analyzed independently. This procedure was chosen because it allowed us to verify any morphological and orientation differences among the analyzed spherulites, and because the total number of objects was not large enough to calculate a statistically meaningful ODF.

For sample D85, it is possible to appreciate symmetry typical of bow-tie aggregates (Figs. 4a and 6a): the symmetry in the pole figures is orthorhombic, but with an axial component as well (Fig. 4a). The axial component becomes stronger in the larger spherulites (Fig. 4b), so it is possible to speculate that new lamellae tend to grow radially with respect to the starting aggregate (as bow-tie morphology, see Fig. 4a), generating a progressively more spherical morphology as more crystals nucleate within the spherulite. The development of the spherulite is characterized by the growth of several bow-ties around a nucleus that form a radial morphology. This is a characteristic shared by all the spherulites, as can be seen in the pole figure with all the 8 spherulite data superimposed (Fig. 4c). This characteristic is also shared by sample D1. In the sample D1, since the total number of object was larger, we selected a representative number of spherulites and we present a comparison of a single spherulite and the pole figure computed from the ODF considering all the lamellae in the sample (Fig. 5a, b). Fig. 5b shows the global pole figure and it is evident that the axial plus orthorhombic symmetries are merged with a stronger axial component.

From the volume renderings of the small spherulite of D85 it is possible to see how the small lamellae started to grow from the biggest one in a radial fashion (see Fig. 4a and Supplementary Movie 1), each one growing with an elongation axis a few degrees from neighboring lamellae (non-crystallographic branching) (Keith and Padden, 1963, 1964). Moreover, the bow-tie morphology is commonly present in the shorter experiments (between 2 and 6 h), while longer duration experiments show dominant radial morphologies. Physical contact of these phases is not likely to depend solely on constitutional undercooling in a boundary layer, but rather develop from heterogeneous nucleation. This
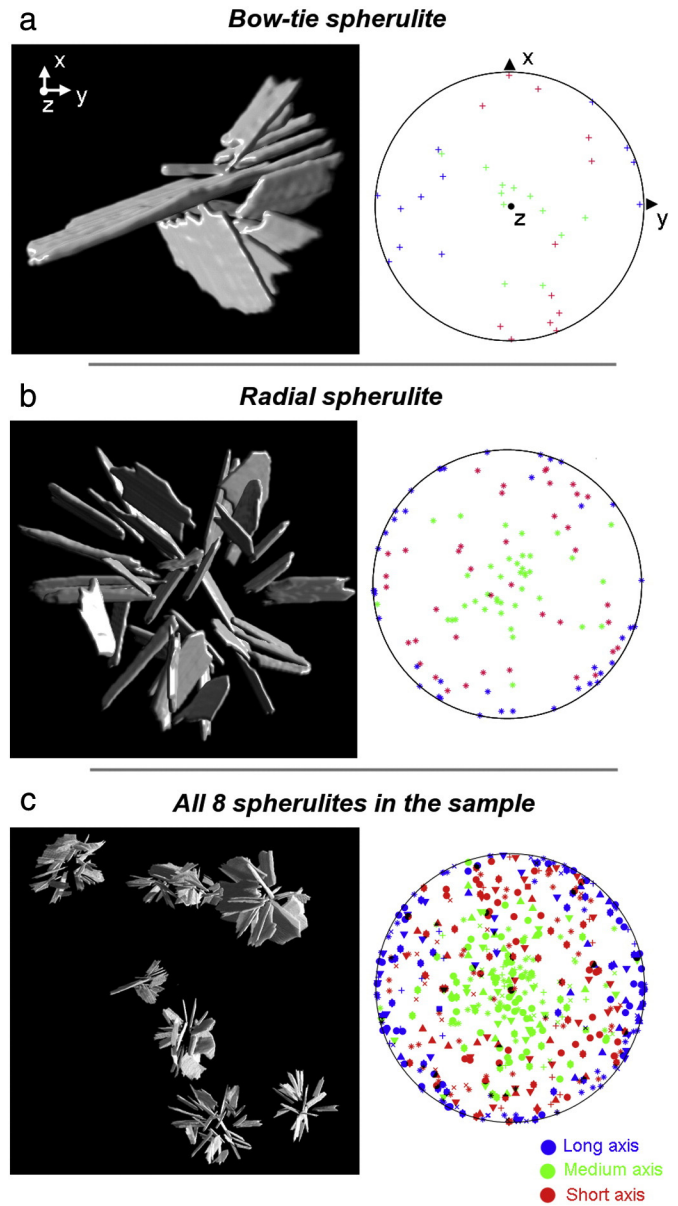

Fig. 4. Sample D85: volume renderings of spherulites and Shape Preferred Orientation (SPO) analyses. SPO analyses have been performed on a synchrotron phase-contrast X-ray computed microtomography dataset. In the pole figures, the long, medium and short axes of the ellipsoids used for fitting the single lamella have been plotted. (a) "Bow-tie" spherulite. (b) The largest spherulite in D85. (c) All the spherulites in D85; in the polar figure, different symbols have been used for the 8 different spherulites.

geometry is not easy to appreciate directly from the 3D rendering in the bigger spherulites, but pole figures can highlight this feature (Fig. 4b–c).

Both 2D images (Figs. 6, 7) and 3D reconstructions (Figs. 4, 5), and EBSD analysis of specimen D85 (Fig. 8) illustrates that spatially heterogeneous nucleation dominated the formation of spherulites. Furthermore, the EBSD analysis focused on potassium feldspar as it is the principal mineral of the spherulites in D85 (ranging from 84.4 to 93.6%). The orientation map (Fig. 8a) shows that each lamella within the spherulite is characterized by different crystal orientations, completing and confirming the results obtained with microtomography. Thus, spherulite in these samples cannot be considered as a single crystal but rather as a radial aggregate of different crystals. In detail, in Fig. 8 we can see groups of crystals with same colors indicating the similar orientation; crystals with red color correspond to orientation with the c-axis parallel to the sample X direction, crystals with the blue
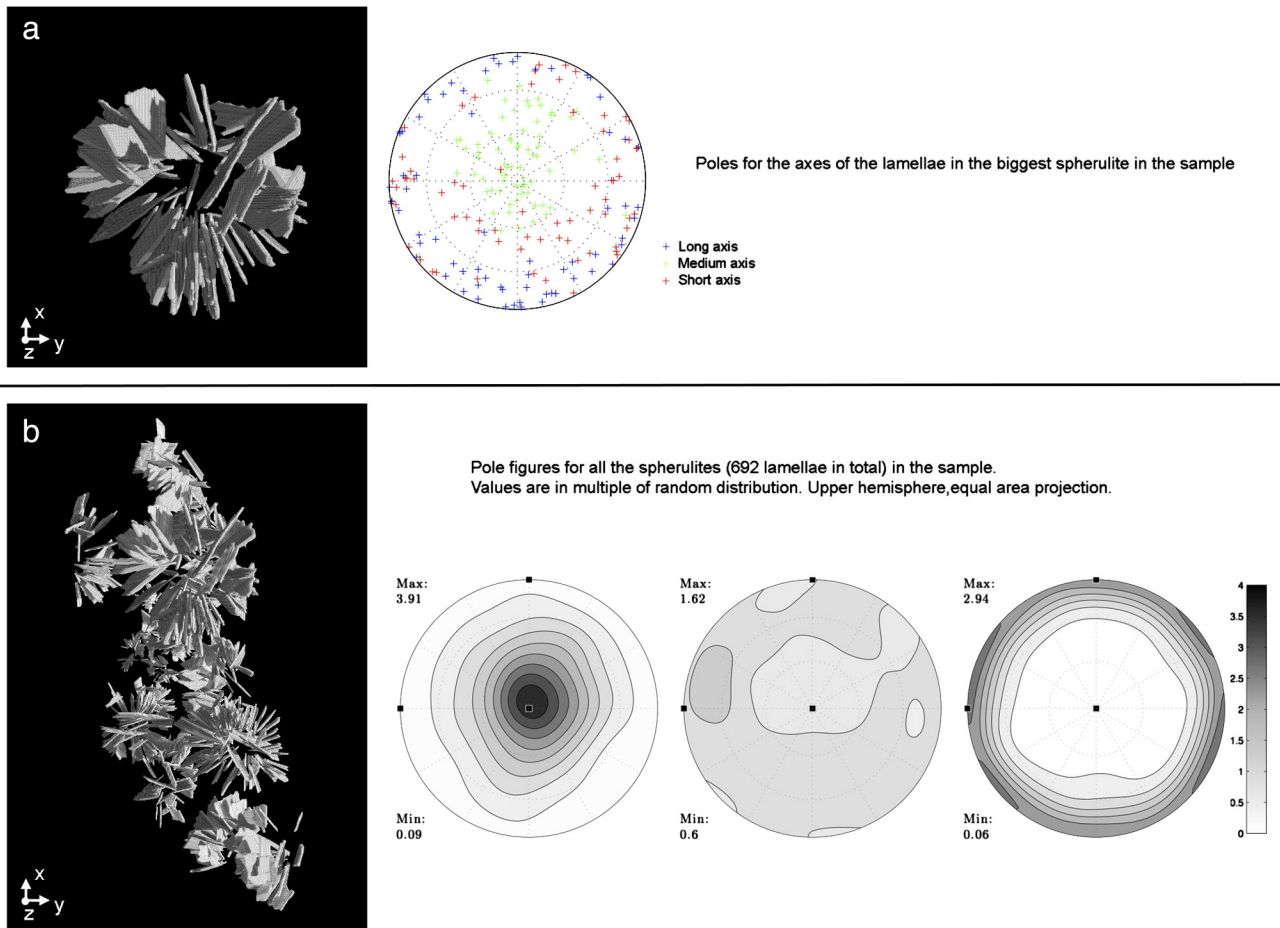
Fig. 5. Sample D1: volume renderings of spherulites, Shape Preferred Orientation (SPO) and shape Orientation Density Function (ODF) analyses. (a) Volume rendering of the largest spherulite in D1 and SPO from phase-contrast X-ray computed microtomography (PC mCT) data. (b) All the spherulites imaged in D1 by PC mCT and the corresponding ODF; from left to right, pole figures show the orientation along medium, short and long axes, respectively.

color have −**a*** or **a*** parallel to the X direction. A high fraction of very long crystals have two colors, indicating the crystals are twinned. Many crystals are very long and straight, but some of them are bent. The plot of the misorientation angle from mean orientation for each grain (Fig. 8b), illustrated that misorientation with grain is locally more that 5° and in fact can reach 35.4° in this spherulite. Such extreme bending of crystals is probably caused by localized plasticity occurring at high temperature. In Fig. 8b the traces of twin boundaries on the sample surface are marked by white lines, and some of these twin boundaries are very straight; others are bent or wavy like the grain boundaries of the crystals, indicating an unstable regime of crystal growth. Furthermore the spatially variable misorientation in the kernel angle misorientation (KAM) plot (Fig. 8b) with strong local misorientation at both terminations of some crystals (indicated by arrow heads), implies that spatially heterogeneous nucleation is dominant during the formation of such morphologies in sample D85.

The crystallographic and statistical analysis of the spherulite is shown in Fig. 9. The pole figures of the crystallographic directions [100], [010] and [001] have a classical distribution known as [001] axial CPO or fiber texture (Fig. 9a), where the [001] directions form a maximum point in the ideal case and the other crystallographic directions are axially distributed about [001] in the form of girdles of [100] and [010]. The double girdles of [100] are caused by twinning and show that twinning is an important aspect of this spherulite. To determine the twin laws operating the correlated misorientation angle histogram (Fig. 9b) and associated rotation axes in crystal coordinates, Fig. 9b provides direct evidence. The correlated misorientation is the description between two neighboring crystals such as the host crystal and

twinned crystal. The correlated misorientation angle histogram (Fig. 9b) has very high frequency of 35% at 180°, which is the twinning misorientation angle for triclinic and monoclinic feldspars (e.g., Smith and Brown, 1988). The plot of the correlated misorientation axes (Fig. 9c) has two maxima, one parallel to **a*** and the other parallel the **c**-axis. From Table 1, the only two twins laws that correspond to axis/angle pairs **a***/180° and **c**/180° are the X and Carlsbad twin laws. However as anorthoclase is monoclinic the two twin laws are symmetrically equivalent. As the two twin laws are two-fold rotational axes, in which both **a*** and **c** are perpendicular to each other and to the monoclinic symmetry two-fold **b**-axis, which is parallel to **b***, it follows that **a*** / 180° + **b*** / 180° = **c** / 180° and **c** / 180° + **b** / 180° = **a*** / 180°. We have confirmed equivalence in MTEX by detecting the X and Carlsbad twin laws in the EBSD maps with either X (**a*** / 180°) or Carlsbad (**c** / 180°) in Fig. 8b shown as white lines. Using the detection of twin boundary lengths we calculated that 38% of the grain boundaries are twins in the spherulite, which is consistent with the double girdle in the [100] pole figure (Fig. 9a), the high misorientation angle frequency at 180° (Fig. 9b) and the high density of misorientation axes at **a*** and **c** (Fig. 9c). Additional confirmation of the twin laws comes the orientation of the traces of the twin planes in the sample plane (Fig. 8) and the orientation of maximum density the **a***(100) pole figure (not illustrated), which is normal to twin traces confirming that the twin plane is **a***(100) as expected in the X or Carlsbad twin law in monoclinic feldspar (e.g., Smith and Brown, 1988).

One of most striking features of the grains in Fig. 8a is the needle-shaped form of most crystals in the 2D section sampled by EBSD. Some crystals (green and blue) elongated normal to the X specimen
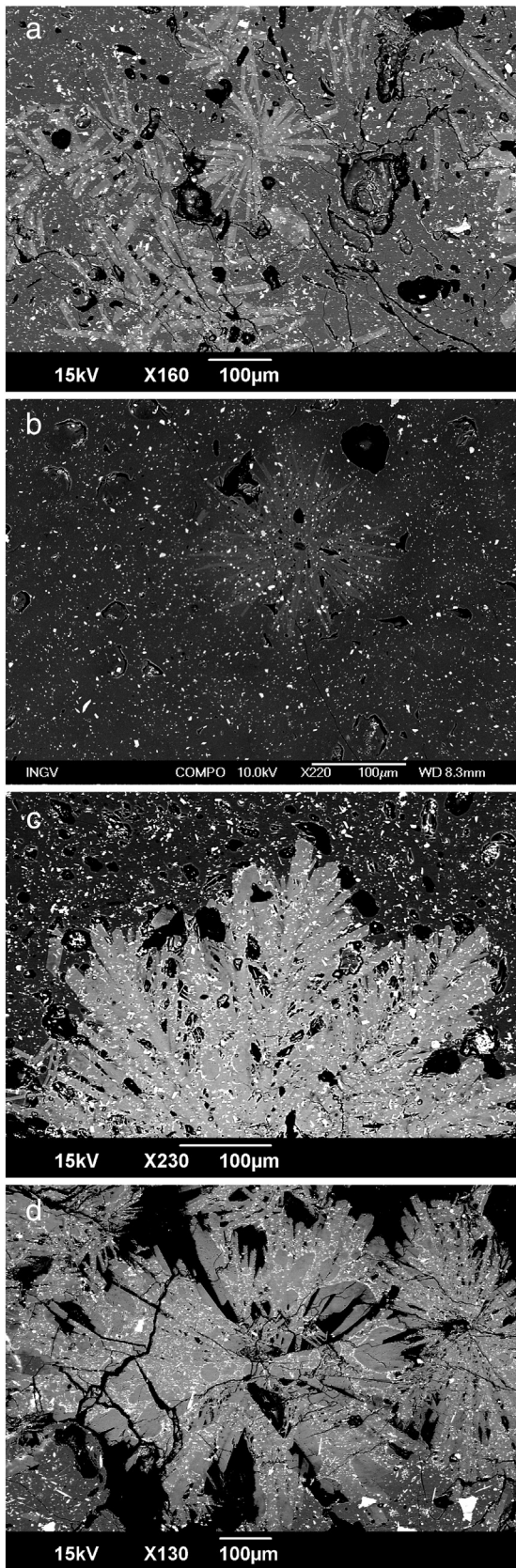
Fig. 6. BSE images of spherulitic morphologies: (a) "bow-tie" spherulite characterized by t_{exp} = 2 h, 150 MPa and ΔT = 42 °C; (b) spherulite with tabular widely spaced crystals at t_{exp} = 2 h, 70 MPa and ΔT = 14 °C; (c) tabular crystals split off from an existing lamella to create branched spherulite characterized by t_{exp} = 8 h, 200 MPa and ΔT = 20 °C; (d) the close denser spherulite from t_{exp} = 14 h, 150 MPa and ΔT = 42 °C.

direction show larger cross-sections corresponding to the lamella shape visualized by 3D microtomography. These large cross-section crystals have a^* or $-a^*$ direction parallel to X in the XY surface of specimen. For the characterization of growth anisotropy it is important to know what are the crystallographic directions of the long axes of the grains. Using 2D EBSD data and MTEX script we can automatically measure the vector corresponding the long axis of the crystals in specimen XY coordinates using the command "principal components", which uses Singular Value Decomposition (SVD) of the grain face coordinates to solve the eigenvectors for long and short directions and this can be converted to 3D vector with the Z component being zero. The grain aspect ratio can be calculated using the command "aspect ratio", using the same SVD method. The mean orientation of the grains (**g**) and specimen 3D vector (**r**) the crystallographic direction (**h**) of the long-axis can be calculated as **h** = inverse(**g**) ∗ **r**, this formula can be applied to one or all grains of anorthoclase. The results can be sorted as a function of aspect ratio and plotted in crystal coordinates (Fig. 9d, e). A plot of all axial ratios shows some spread in orientations with a peak parallel to the **c**-axis of 7 multiples of a uniform distribution (MUD). For grains with axial ratio of 8 or more the peak parallel to the **c**-axis of 52 MUD; the peak is higher because fewer crystals have a very high axial ratio, but the largest axial ratio in this sample is 48.9. In previous reports of axial ratios of alkali feldspars nucleation in hydrous melts (e.g., Fenn, 1977), the relative elongation directions are **a** > **c** > **b**. We can compare this with **c**-axis clearly the long-axis direction in the XY plane (Fig. 9d, e), and the large-cross section lamella seen in (Fig. 8a) have **a**∗ parallel to X and long axis normal to X in the XY plane, which is parallel to **c**-axis, hence the large crystal face (blue or green due to twinning) must be near to **b**∗ / **b**. Hence we deduce that the long, intermediate and short axes of the large-cross section lamella crystal are **c** > **a**∗ > **b**∗ / **b**. A more accurate individual analysis can be made by plotting the pole figures of individual large-cross section lamella crystals. These crystals have **a**-axis parallel to X and **b**∗ / **b** is parallel to Z and **c**∗ is close to Y, hence **c**∗ > **a** > **b**∗ / **b**. The angles between **a** and **a**∗ and **c** and **c**∗ are both 26.1°. The crystals with large-cross section faces represent an important area fraction of about 5% (Fig. 8a) and hence they also contribute strongly to the pole figures in Fig. 9a. The main peak in the [010] pole is parallel to the XY specimen surface normal to Z, indicating that the crystal faces with large surface areas are statistically **b**∗, and this in general agreement with previous work (e.g., Fenn, 1977). The main difference with previous work is the relative position of long axes either **a** > **c** > **b** / **b**∗ (Fenn, 1977) or this study with **c** > **a**∗ > **b** / **b**∗ from statistical measurements (pole figures, axial ratios in XY plane) based on 3179 grains or **c**∗ > **a** > **b**∗ / **b** from two individual grains. The number of grains measured with 2D EBSD (3179 grains) in one spherulite can be compared with less than 50 in 3D microtomography (Fig. 4) on sample D85. The presence of all small grains in the 2D EBSD maps (Fig. 8) shows a more complex distribution of crystal shapes than detected by 3D microtomography (Fig. 4). When comparing the EBSD maps (Fig. 8) with pole figures in Fig. 9a, the **c**-axial CPO should give rise to the so-called "bow-tie" spherulite crystal morphology (e.g., Fenn, 1977; Lofgren, 1974; Swanson, 1977).

Three kinds of spherulitic shapes occurred in the experimental runs: (i) "bow-tie" spherulites (Figs. 4a, 6a and 7a, Supplementary Movie 1) grown at low ΔT, are more easily identified in the initial stage of crystallization, and they are present commonly in short duration experiments (2–6 h); (ii) open radially distributed spherulites with widely spaced crystals (Fig. 6b) grown at low ΔT (between ~15 and 40 °C) and short experimental durations (2–6 h) (iii) close spherulites consisting of tabular crystals radially and densely aggregated (Figs. 6c, d and 7b, c, e, f), formed at higher ΔT (between 40 and 70 °C) and at long experimental time (>6 h), in agreement with previous observations (Keith and Padden, 1963; Lofgren, 1971a).

An individual branch type form spherulites: tabular shape (see Figs. 4, 7). The low/intermediate ΔT favored the development of tabular crystals in spherulites in agreement with Lofgren (1974), so it controls
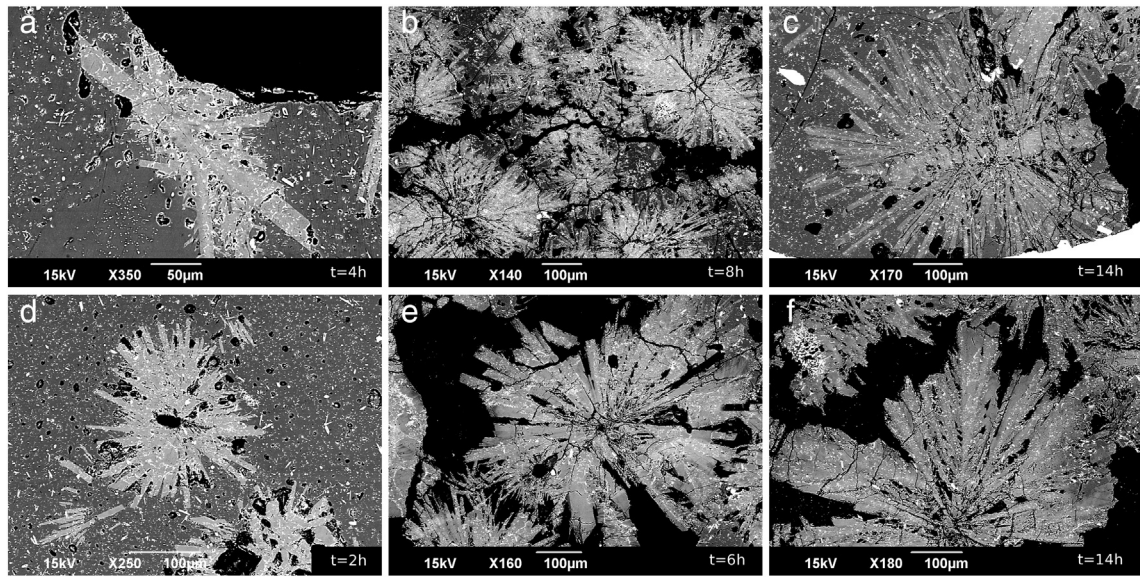
Fig. 7. BSE images of spherulites with crystal (a, b, c) and bubble (d, e, f) as a nucleus. Spherulites characterized by the transition from a single crystal with incipient bow-tie formation (a) into a radial spherulite (b, c). (a) Experimental condition: $t_{exp} = 4$ h, 100 MPa and $\Delta T = 19$ °C; (b) experimental condition: $t_{exp} = 8$ h, 200 MPa and $\Delta T = 20$ °C; (c) experimental condition: $t_{exp} = 14$ h, 150 MPa and $\Delta T = 42$ °C. (d, e, f) Evolution of spherulitic morphology with time, from open spherulite (d) to closed spherulites (e, f). (d) Experimental condition: $t_{exp} = 2$ h, 100 MPa and $\Delta T = 69$ °C; (e) experimental condition: $t_{exp} = 6$ h, 100 MPa and $\Delta T = 69$ °C; (f) experimental condition: $t_{exp} = 14$ h, 100 MPa and $\Delta T = 69$ °C.

the morphology of the single crystal that nucleates and grows within the spherulite. Tabular crystals are ubiquitous in spherulites at different experimental conditions.

Nuclei of these radial morphologies are crystals or bubbles (see Figs. 6, 7), therefore the spherulite has to be considered an aggregate of several tabular alkali feldspars nucleating and growing on a pre-existing surface. Several samples show spherulites with a large crystal as nucleus, where lamellae are arranged radially around it (see Fig. 7a, b, c). In some cases, we recognized the beginning of the process of heterogeneous nucleation, where lamellae begin to nucleate
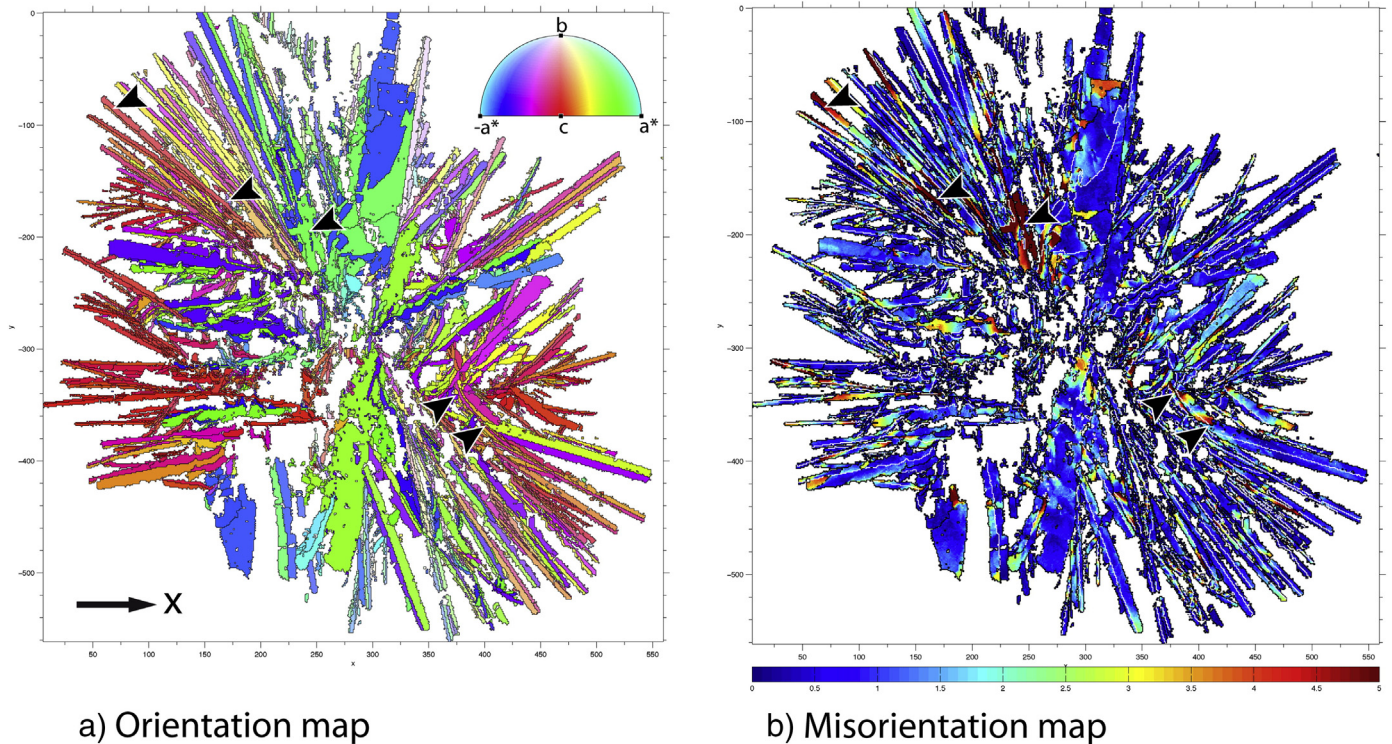

Fig. 8. EBSD maps of potassium feldspar (anorthoclase) in a spherulite in sample D85. (a) Orientation map where the mean orientation of each grain has a color based on the crystal direction that is parallel to the specimen X direction. The color code is shown in the inset at the top right, with main crystallographic directions for monoclinic symmetry. (b) Misorientation map of the misorientation from mean crystal orientation expressed as color code with angles between 0° and 5°. Angles higher than 5° are shown as though they are 5° to emphasis the lower angles. The maximum misorientation angle in this map is 33.9°. Black arrows illustrate regions of high misorientation angles and crystal bending at both ends of the crystals in specific cases.
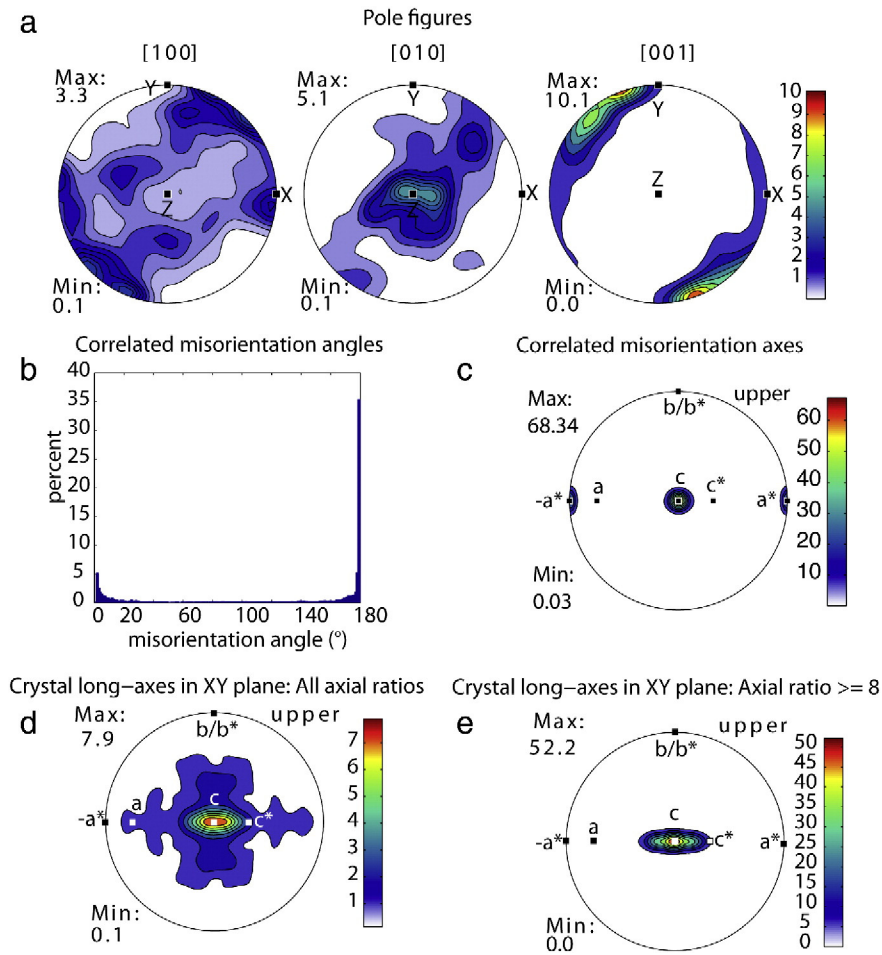
Fig. 9. EBSD pole figures, misorientation angles and axes and axial ratios in the XY plane of potassium feldspar anorthoclase crystal in sample D85. (a) Lower hemisphere equal area projection pole figures of [100], [010] and [001], with specimen X, Y, Z directions marked by black squares. (b) Histogram of frequency correlated misorientation angles in percent as a function of angle. Lower angles represent misorientation within crystals and high angles near 180° represent twins. (c) Upper hemisphere equal area projection in crystal coordinates of correlated misorientation axes. The crystallographic directions (**a**, **a***, **b**, **b***, **c**, **c***) for monoclinic symmetry are marked by black or white squares. Note high densities parallel to **a*** and **c**. (d) and (e) Upper hemisphere equal area projection in crystal coordinates of the direction of the crystal long-axes in XY plane. Figure (d) is for all axial ratios including crystals with circular shape with axial ratio of one in 2D and crystals with the highest axial ratio of 34.4. Figure (e) is for axial ratios greater or equal to 8. Note high densities in region of **c** and **c***.

on the pre-existing crystal, forming bow-ties (Fig. 7a) and radially distributed shapes (Fig. 7b and c). Increasing the experimental duration drives the transition from single crystal to bow-tie to radial spherulite through heterogeneous nucleation. Between 8 and 16 h

Table 1
Table of twins for monoclinic alkali feldspars.

Twin law	Twin axis	Symmetrically equivalent twin
Normal twins		
X	**a*** ⊥ (100)	Carlsbad
Manebach	**c*** ⊥ (001)	Ala
Prism (110)	⊥ (110)	
Prism (130)	⊥ (130)	
Braveno	⊥ (021)	
Cunnerdorf	⊥ ($\bar{2}$01)	
Unnamed	⊥ (111)	
Breithaupt	⊥ ($\bar{1}$11)	
Goodsprings	⊥ ($\bar{1}$12)	
Parallel twins		
Ala	**a** [100]	Manebach
Carlsbad	**c** [001]	X
Petschu	[1$\bar{1}$0]	
Nevada	[$\bar{1}$12]	

Note: * = reciprocal lattice; ‖ = parallel to; ⊥ = normal to plane.
Misorientation for all twins is 180°.

heterogeneous nucleation favored the secondary branching, tabular crystals that nucleate on an existing lamella to create branched spherulites (see Figs. 6c and 7f). Furthermore, the core of spherulites can be a bubble (Figs. 6b and 7d, e, f), therefore the surface of bubbles may aid the formation of these radial morphologies, providing nucleation points (Arzilli and Carroll, 2013; Clay et al., 2012; Davis and Ihinger, 1998; Gimeno, 2003; Shelley, 1993).

Results of EBSD analysis (Fig. 9) show that only Carlsbad twins are present in the spherulites. Twinning in feldspar is generally a result of deformation or growth (Buerger, 1945). Carlsbad twins are produced only by growth (e.g., Smith and Brown, 1988) through an accidental, non-random misalignment of atoms attaching to a crystalline substrate during the incipient stages of crystallization. In the early stage of nucleation when the nucleus is stable, atoms can rapidly attach to the crystal face favoring growth twinning defects in the crystal structures and thus rapid crystal nucleation and growth may play a crucial role in controlling the mechanism(s) of spherulite formation.

3.3. Role of superheating

The growth of spherulites at high ΔT and high melt-viscosity (low H_2O content) is well established by several studies (Keith and Padden, 1963; Lofgren, 1974; Magill, 2001; Swanson, 1977), whereas the experiments of Arzilli and Carroll (2013) show that these morphologies can develop even at low ΔT. The results of Arzilli and Carroll (2013)

demonstrate that ΔT is not the unique driving force for spherulitic crystallization because −ΔT, pressure and water content can influence spherulite formation. However, these morphologies can be perturbed by heterogeneities (either microcrystals or the surfaces of the bubbles which can act as a nucleus, promoting heterogeneous nucleation in the spherulites), yielding a rich variety of polycrystalline growth patterns (Gránásy et al., 2004; Keith and Padden, 1963, 1964). An important aspect to consider for better understanding spherulitic crystallization is the initial period of the experiment (2–3 h) above the liquidus of alkali feldspar. Arzilli and Carroll (2013) show that the trachytic melt produced spherulites after high superheating conditions, whereas they did not appear after low superheating (conditions at a few degrees above the liquidus). In fact, Fig. 3 shows that no spherulitic growth was observed at 30–50 MPa (except D81) and in just a few experiments at 70 and 100 MPa since they were characterized by a low superheating (<60 °C), favoring tabular crystals. Our observations suggest that high values of superheating favor the destruction of potential heterogeneities that could serve as nucleation sites. The combination of high superheating and low ΔT is thermodynamically unfavorable to nucleation (Arzilli and Carroll, 2013), resulting in low crystal nucleation densities, and in some cases leading to spherulitic growth. Furthermore, spherulites grown at low undercooling are characterized by crystals with tabular shape (Figs. 4, 7), and not by crystals with acicular shape as observed at high undercooling (Lofgren, 1971a). During the initial melting period at high superheating it appears that many nuclei were destroyed, rendering homogeneous nucleation more difficult at lower undercooling conditions. After the initial melting period, the few new crystals formed at low ΔT and the walls of the bubbles were able to induce the heterogeneous nucleation of the alkali feldspar, triggering the spherulitic growth. It has been suggested that the crystal branching was induced by heterogeneous nucleation and variation of the crystallographic misorientation-dependent interfacial energy (σ) according to the theoretical studies of Gránásy et al. (2004, 2005). We should be careful to distinguish between crystal–crystal interfaces between two adjacent crystals of the same mineral, crystal–crystal interfaces between two adjacent crystals of the different minerals, and crystal–melt in situ conditions, now preserved as crystal–melt interfaces. In this study we have focused our attention only on anorthoclase. A high fraction of anorthoclase crystals contain median twin boundaries that divide the crystal into equal parts, some of which are bent or curvy providing regions for nucleation; where bending would result in a variation of local dislocation density (e.g., Ashby, 1970) and interfacial twin plane curvature will result in a variation in the misorientation-dependent interfacial energy (Gránásy et al., 2005). A twin boundary is considered to be a special type of crystal interface with a very specific misorientation relationship between host and twin (see Table 1), and in addition a specific twin plane, which separates the crystal into host and twin (e.g., **a***(100) for Carlsbad and X twin laws in monoclinic feldspar). The twin plane may have a lower energy than general crystal–crystal boundaries (e.g., Sutton and Balluffi, 1998), and hence reduce the energy budget of the twinned crystal, favoring its formation. Many of the long crystal face traces in the XY specimen section must also be parallel to **a***(100) (Figs. 8 and 9). It is known that the grain boundary energies and the areas of boundaries are inversely correlated (Li et al., 2009), hence we would expect long boundary traces in 2D to correspond to low energy interfaces, which strongly suggests that the twin plane **a***(100) has low energy in anorthoclase. It is also true that longest length of traces of crystal (external) faces is also parallel to **a***(100), although the matter in contact could be another crystal, another mineral or even glass. Hence it appears that surface energy in the **a***(100) plane is probably also quite low. Whereas the crystal (external) faces nearly normal to the **c**-axis have very short boundary traces and hence must have much higher surface energy than **a***(100). From the estimates of crystal long axes and length of traces of crystal faces we can infer the surface and probably the interfacial energy must be very anisotropic in anorthoclase. The morphological transition, from widely spaced

crystals to denser spherulites, can occur by reducing the σ anisotropy according to Gránásy et al. (2004), thus favoring heterogeneous nucleation on preexisting crystal faces. Here we show that the high superheating and low undercooling have a morphological control on the crystal shapes, in agreement with previous studies (Arzilli and Carroll, 2013; Corrigan, 1982; Dinel et al., 2008; Lofgren, 1974). In fact, Corrigan (1982) suggested that the increase of the superheating allows displacement of the spherulitic field boundaries to smaller ΔT values. Furthermore, Dinel et al. (2008) showed that spherulitic growth could occur in the cores of dacitic pillow lobes through a rapid cooling of a superheated melt. In conclusion, the superheating of the magma before the eruption could be one of the processes that promote the formation of spherulites.

3.4. Growth rates of alkali feldspars within spherulite

Time is an important variable for the development of spherulites, as indicated by the fact that the experimental duration affects spherulite size. Time and the growth rate of the spherulites are issues debated by several authors (Baker and Freda, 2001; Castro et al., 2008; Fenn, 1977; Lofgren, 1971a; Swanson, 1977; Watkins et al., 2009). Although 2D shape measurement using BSE images gives us an important estimation of the crystal size and growth rate, the measurements of 3D shape and volume of crystals are of much greater scientific significance. Being able to obtain the 3D shape of feldspars within spherulites and knowing the duration of growth (experimental duration), we were able to calculate the growth rate in volumetric terms. This is the first time that the growth rate of feldspars has been calculated by considering the volume of crystals. The volumetric growth rate (Y_V) of alkali feldspar within spherulites ranges from 10^{-11} to 10^{-14} cm³/s (see Table 2). Four orders of magnitude of Y_V are due to the different sizes of feldspars; larger crystals of spherulites could be nucleated at the beginning of the experiment, whereas smaller crystals may be nucleated later. Therefore, 10^{-11} and 10^{-12} cm³/s are the maximum growth rates of alkali feldspar, whereas 10^{-13} and 10^{-14} cm³/s could be underestimated values. This means that with the maximum Y_V, the lamellae of the spherulite can reach a volume of ~10 μm³ in 1 s.

In this study, we also measured the growth rate related to the maximum axis length. The maximum growth rates (Y_{L3D}) obtained from 3D approach are: 2.4×10^{-6} cm/s for D1 and 1.4×10^{-6} cm/s for D85 (see Table 2). We measured also the maximum length of crystals using 2D images in order to estimate the growth rate (Y_{L2D}). The estimated Y_{L2D} of alkali feldspar in the spherulites ranges between 10^{-6} and 10^{-7} cm/s (see Fig. 10a, b and Supplementary Table 2). The maximum growth rate for D1 is 1.14×10^{-6} cm/s, whereas for D85 is 9.30×10^{-7} cm/s. The comparison between 2D and 3D linear measurements of growth rate (Y_{L3D} vs Y_{L2D}) shows that the 2D approach slightly underestimates the growth kinetics.

By taking into account similar experimental durations, the orders of magnitude of Y_{L2D} (from 10^{-6} to 10^{-7} cm/s) are comparable with growth rates (from 10^{-6} to 10^{-8} cm/s) estimated from previous studies (Baker and Freda, 2001; Castro et al., 2008; Fenn, 1977; Lofgren, 1971a; Swanson, 1977). This suggests that the growth rates of the feldspar spherulites may not depend strongly on melt composition.

Fig. 10a and b shows the growth rates (Y_{L2D}) of spherulites as a function of experimental duration. In both cooling and "cooling + decompression" experiments, Y_{L2D} decreases with increasing time. The diameter of spherulites increase with the experimental duration, implying continuous growth, at least over the time scales investigated (up to 14 h), although the rate tends to decrease with time. Furthermore, experiments characterized by high ΔT and low superheating show low growth rates (10^{-7} cm/s) (see Fig. 10a). This result confirms that low temperature conditions (high ΔT) could favor a slow growth of spherulites in agreement with Castro et al. (2008).

An interesting comparison between the growth rates (Y_{L2D}) of alkali feldspars within spherulites and those of single crystals (calculated from Arzilli and Carroll, 2013) can be made. In particular, this comparison

Table 2
Results of growth rates of alkali feldspar within spherulites using 3D images.

Sample	V (cm³)	Y_V (cm³/s)	Y_V min (cm³/s)	Y_V max (cm³/s)	Y_V average (cm³/s)	L_{3D} (cm)	Y_{L3D} (cm/s)	Y_{L3D} min (cm/s)	Y_{L3D} max (cm/s)	Y_{L3D} average (cm/s)
D85	4.1E−07 (9)	9E−12 (1)	5.35E−14	1.38E−11	1.61E−12	3.0E−02 (3)	1.4E−06 (1)	2.70E−07	1.65E−06	7.55E−07
D1	3.5E−07 (6)	1.2E−11 (2)	1.50E−14	1.58E−11	1.95E−12	3,5E−02 (2)	2.4E−06 (1)	1.69E−07	2.64E−06	1.05E−06

Note: V = average volume of the 10 largest lamellae; Y_V = volumetric growth rate measured using the 10 largest lamellae; Y_V min and Y_V max show the minimum and the maximum value of volumetric growth rate, respectively; Y_V avarage = the avarage value of volumetric growth rate obtained taking into account 180 lamellae for D85 and 694 lamellae for D1; L_{3D} = average length of the 10 largest lamellae; Y_{L3D} = growth rate measured using the 10 largest lamellae; Y_{L3D} min and Y_{L3D} max show the minimum and the maximum value of growth rate, respectively; Y_{L3D} avarage = the avarage value of growth rate obtained taking into account the length of 180 lamellae for D85 and 694 lamellae for D1. The value in parentheses is the standard deviation of the mean value.

highlights the different growth rate between a single crystal and a lamella nucleated within spherulite. The comparison shows that the growth rate of the largest alkali feldspar in spherulites is either similar or higher than that for single crystals by up to one order of magnitude. By considering the same experimental time, the maximum length (L_{2D}) of the lamellae is slightly larger than the single crystals of alkali feldspar. Therefore, it is reasonable to hypothesize that lamellae have a preferred crystallographic direction of growth with respect to single crystals. In fact, the shape of

lamella shows a main growth direction from the center (heterogeneous nucleation) to the spherulite front. The present study highlights that **c** rather than **a** is the crystallographic axis direction (cf. Fenn, 1977) more developed in lamellae of spherulites.

4. Conclusions and implications

The combination of PC mCT and phase-retrieval processing allowed us to separate alkali feldspars from the trachytic glass. The phase retrieval approach proved to dramatically increase the data quality from a segmentation point of view, especially for those samples in which the absorption contrast was low. Therefore, the single-distance phase retrieval algorithms can be used in samples where a better contrast of the different phases is needed, and in situations far from the ideal ones required by the theory. Since the experimental setup has no special requirements, as might be needed for multiple-distance phase retrieval algorithms or holotomography, single-distance phase retrieval processing will be an important tool for geologist to study rock textures.

This approach allowed us to study the shape-preferred orientation of lamellae within the spherulites. A further step was the comparison of information about SPO with CPO data from 2D EBSD to complement the results, trying to correlate the morphology with crystallographic directions. The EBSD data provides evidence for strong CPO and a high number of twinned grains. A twin boundary is considered to be special type of grain boundary, which may have a lower energy than general grain boundaries, and hence reduce the energy budget of the twinned crystal. Many of the twinned grains show evidence of strong local bending as shown by the KAM plot at the extremities of the crystals, which combined with twins creates local sites for heterogeneous nucleation. We obtained important information about nucleation mechanism, which seems to start with a heterogeneous nucleus subsequently evolving as "bow tie" aggregates, developing radially dense spherulitic morphologies in few hours. Therefore, the time drives the transition from a single crystal into a polycrystalline aggregates (Fig. 7a, b and c, Supplementary Movie 2), reaching densely branched morphologies (Fig. 6c, d). The morphology of single crystal of the spherulite is controlled by ΔT, tabular morphology is dominant.

Our results show that the development of the spherulite is dominated by heterogeneous nucleation and the growth can occur in a short time in water saturated trachytic melts, reaching ~400 μm diameter in a few hours. Furthermore, if the magma is superheated, spherulitic crystallization can occur in subliquidus conditions at low/intermediate ΔT, after an event of cooling or decompression, implying that the spherulitic crystallization can occur in subliquidus conditions. Therefore, spherulites are not necessarily limited to being products of devitrification in subsolidus conditions, close to the glass transition. These results show that the nucleation and growth of spherulites in trachytic or rhyolitic obsidian could occur at pre-eruptive temperature conditions.

The study here reported has several implications, both in terms of scientific and technological advancements. First of all, in addition to showing the first 3D analysis of spherulites in trachytic melts, the P–T conditions of spherulites formation may have particular relevance for another much-debated process: the origin of orbicular textures in granitic rocks (spherical bodies of radiating crystals, in a normal
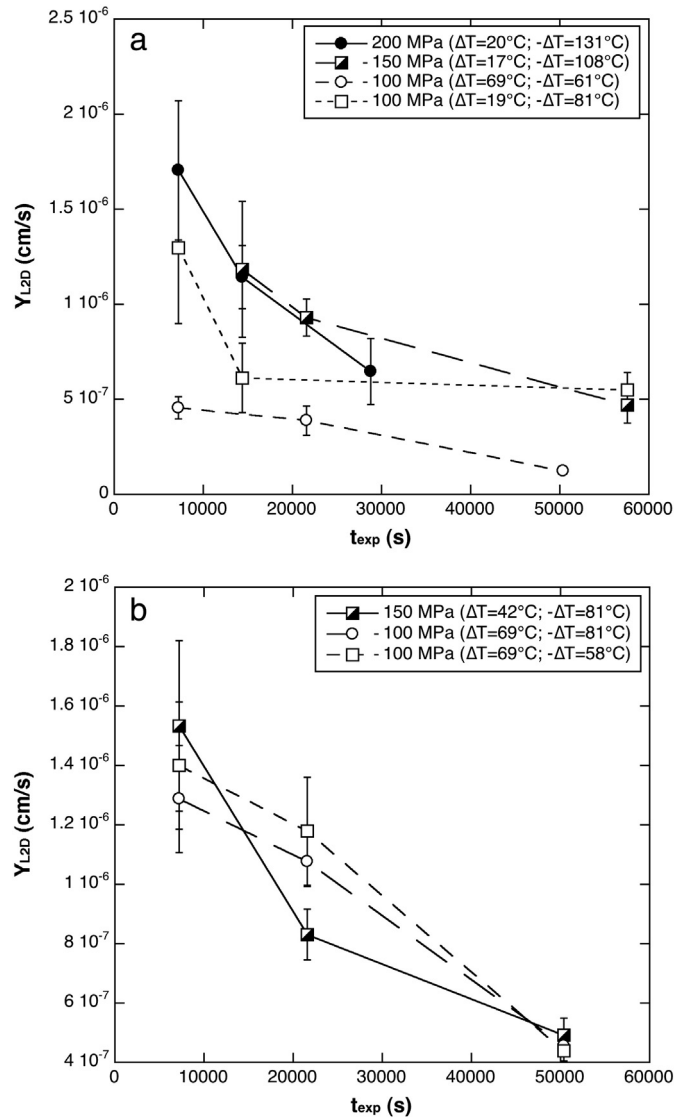

Fig. 10. (a) Relation between growth rate (Y_{2D}) of alkali feldspar spherulite and experimental time (t_{exp}) for cooling experiments. (b) Relation between growth rate (Y_{2D}) of alkali feldspar spherulite and experimental time (t_{exp}) for "cooling + decompression" experiments. The growth rate was estimated measuring the 10 largest lamellae within the spherulite, using BSE images (2D approach).

equigranular matrix). As shown by Burnham and Davis (1974), the isothermal ascent (decompression) of a water-undersaturated near-eutectic melt will result in superheating as pressure decreases, until the rising melt intersects the wet solidus at some lower pressure, determined by the original melt water content. Our results demonstrate that such superheated melts, even when subjected to relatively small undercoolings, are capable of producing spherulitic textures, and in a shallow plutonic environment, these textures could evolve to form orbicular granitic rocks. Such near-liquidus crystallization from super-heated nuclei-poor melts to produce orbicular textures has been proposed by others (e.g., Ort, 1992; Vernon, 1985), but our experimental data are the first to demonstrate spherulitic growth at near-liquidus conditions, as required by such proposals to explain orbicular textures. Superheating conditions in natural magmas are rare and it is difficult to find evidence of superheated melts but the results of this study could be applicable to orbicular textures in intrusive igneous rocks (such as syenite, monzodiorite and granodiorite). Orbicular granites can crystallize at high P and H_2O (condition at depth) (Decitre et al., 2002; Durant and Fowler, 2002; Elliston, 1984; Leveson, 1966; Lindh and Näsström, 2006; Ort, 1992; Smillie and Turnbull, 2014; Sylvester, 2011; Symes et al., 1987; (Vernon, 1985), therefore these experiments could reproduce their crystallization conditions in intrusive rocks. Several authors claim that superheated melts can produce orbicular textures (Decitre et al., 2002; Lindh and Näsström, 2006; Ort, 1992; Smillie and Turnbull, 2014; Sylvester, 2011; Vernon, 1985) and the present study provides experimental evidence to the claims cited above.

The results of our study can be also useful in the context of laboratory experiments to better understand the behavior of superheated starting materials during crystallization. Many authors used superheating conditions as starting experimental conditions (e.g., Arzilli and Carroll, 2013; Brugger and Hammer, 2010; Conte et al., 2006; Iezzi et al., 2008, 2011; Lofgren, 1983; Pupier et al., 2007; Vetere et al., 2013; Vona and Romano, 2013; Vona et al., 2011) but few of them studied its effect on nucleation and crystal growth (e.g., Arzilli and Carroll, 2013; Vetere et al., 2013).

Supplementary data to this article can be found online at http://dx.doi.org/10.1016/j.lithos.2014.12.003.

Acknowledgements

References

Arzilli, F., Carroll, M.R., 2013. Crystallization kinetics of alkali feldspars in cooling and decompression-induced crystallization experiments in trachytic melt. Contributions to Mineralogy and Petrology 166, 1011–1027. http://dx.doi.org/10.1007/s00410-013-0906-1.

Ashby, M.F., 1970. The deformation of plastically non-homogeneous materials. Philosophical Magazine 21, 399–424.

Bachmann, F., Hielscher, H., Jupp, P.E., Pantleon, W., Schaeben, H., Wegert, E., 2010. Inferential statistics of electron backscatter diffraction data from within individual crystalline grains. Journal of Applied Crystallography 43, 1338–1355.

Bachmann, F., Hielscher, R., Schaeben, H., 2011. Grain detection from 2d and 3d EBSD data — specification of the MTEX algorithm. Ultramicroscopy 111, 1720–1733.

Baker, D.R., Freda, C., 2001. Eutectic crystallization in the undercooled orthoclase–quartz–H_2O system: experiments and simulations. European Journal of Mineralogy 13, 453–466. http://dx.doi.org/10.1127/0935-1221/2001/0013-0453.

Baker, D.R., Mancini, L., Polacci, M., Higgins, M.D., Gualda, G.A.R., Hill, R.J., Rivers, M.L., 2012. An introduction to the application of X-ray microtomography to the three-dimensional study of igneous rocks. Lithos 148, 262–276. http://dx.doi.org/10.1016/j.lithos.2012.06.008.

Breitkreuz, C., 2013. Spherulites and lithophysae—200 years of investigation on high-temperature crystallization domains in silica-rich volcanic rocks. Bulletin of Volcanology 75, 705.

Brugger, C.R., Hammer, J.E., 2010. Crystallization kinetics in continuous decompression experiments: implications for interpreting natural magma ascent processes. Journal of Petrology 51, 1941–1965. http://dx.doi.org/10.1093/petrology/egq044.

Buerger, M.J., 1945. The genesis of twin crystals. Journal of the Mineralogical Society of America 30, 469–482.

Burnham, C.W., Davis, N.F., 1974. The role of H_2O in silicate melts: II. Thermodynamic and phase relations in the system $NaAlSi_3O_8$–H_2O to 10 kilobars, 700° to 1100 °C. American Journal of Science 274, 902–940. http://dx.doi.org/10.2475/ajs.274.8.902.

Castro, J.M., Beck, P., Tuffen, H., Nichols, A.R., Dingwell, D.B., Martin, M.C., 2008. Timescales of spherulite crystallization in obsidian inferred from water concentration profiles. American Mineralogist 93, 1816–1822. http://dx.doi.org/10.2138/am.2008.2904.

Clay, P.L., O'Driscoll, B., Gertisser, R., Busemann, H., Sherlock, S.C., Kelley, S.P., 2012. Textural characterization, major and volatile element quantification and Ar–Ar systematics of spherulites in the Rocche Rosse obsidian flow, Lipari, Aeolian Islands: a temperature continuum growth model. Contributions to Mineralogy and Petrology 165, 373–395.

Cloetens, P., Barrett, R., Baruchel, J., Guigay, J.P., Schlenker, M., 1996. Phase objects in synchrotron radiation hard X-ray imaging. Journal of Physics D 29, 133–146. http://dx.doi.org/10.1088/0022-3727/29/1/023.

Conte, A.M., Perinelli, C., Trigila, R., 2006. Cooling kinetics experiments on different Stromboli lavas: effects on crystal morphologies and phases composition. Journal of Volcanology and Geothermal Research 155, 179–200. http://dx.doi.org/10.1016/j.jvolgeores.2006.03.025.

Corrigan, G., 1982. The crystal morphology of plagioclase feldspar produced during iso-thermal supercooling and constant rate cooling experiments. Mineralogical Magazine 46, 433–439. http://dx.doi.org/10.1180/minmag.1982.046.341.04.

Couch, S., 2003. Experimental investigation of crystallization kinetics in a haplogranite system. American Mineralogist 88, 1471–1485.

Davis, M.J., Ihinger, P.D., 1998. Heterogeneous crystal nucleation on bubbles in silicate melt. American Mineralogist 83, 1008–1015.

Decitre, S., Gasquet, D., Marignac, C., 2002. Genesis of orbicular granitic rocks from the Ploumanac'h Plutonic Complex (Brittany, France): petrographical, mineralogical and geochemical constraints. European Journal of Mineralogy 14, 715–731.

Dinel, E., Saumur, B.M., Fowler, A.D., 2008. Spherulitic aphyric pillow-lobe metatholeiitic dacite lava of the Timmins Area, Ontario, Canada: a new Archean facies formed from superheated melts. Economic Geology 103, 1365–1378. http://dx.doi.org/10.2113/gsecongeo.103.6.1365.

Dunbar, N.W., Jacobs, G.K., Naney, M.T., 1995. Crystallization processes in an artificial magma: variation in crystal shape, growth rate and composition with melt history. Contributions to Mineralogy and Petrology 120, 412–425.

Durant, D.G., Fowler, A.D., 2002. Origin of reverse zoning in branching orthopyroxene and acicular plagioclase in orbicular diorite, Fisher Lake, California. Mineralogical Magazine 66, 1003–1019.

Elliston, J.N., 1984. Orbicules: An Indication of the Crystallisation of Hydrosilicates, I. Earth-Science Reoiews. 20, 265–344.

Fenn, P.M., 1977. The nucleation and growth of alkali feldspars from hydrous melts. Canadian Mineralogist 15, 135–161.

Gimeno, D., 2003. Devitrification of natural rhyolitic obsidian glasses: petrographic and microstructural study (SEM + EDS) of recent (Lipari island) and ancient (Sarrabus, SE Sardinia) samples. Journal of Non-Crystalline Solids 323, 84–90. http://dx.doi.org/10.1016/S0022-3093(03)00294-1.

Gránásy, L., Pusztai, T., Borzsonyi, T., Warren, J.A., Douglas, J.F., 2004. A general mechanism of polycrystalline growth. Nature Materials 3, 645–650. http://dx.doi.org/10.1038/nmat1190.

Gránásy, L., Pusztai, T., Tegze, G., Warren, J.A., Douglas, J.F., 2005. Growth and form of spherulites. Physical Review E 72, 011605. http://dx.doi.org/10.1103/PhysRevE.72.011605.

Herman, G.T., 1980. Image Reconstruction from Projections: The Fundamentals of Computerized Tomography. Academic Press, New York.

Hielscher, R., Schaeben, H., 2008. A novel pole figure inversion method: specification of the MTEX algorithm. Journal of Applied Crystallography 41, 1024–1037. http://dx.doi.org/10.1107/S002188980 8030112.

Iezzi, G., Mollo, S., Ventura, G., Cavallo, A., Romano, C., 2008. Experimental solidification of anhydrous latitic and trachytic melts at different cooling rates: the role of nucleation kinetics. Chemical Geology 253, 91–101.

Iezzi, G., Mollo, S., Torresi, G., Ventura, G., Cavallo, A., Scarlato, P., 2011. Experimental solidification of an andesitic melt by cooling. Chemical Geology 283, 261–273.

Keith, H.D., Padden, F.J., 1963. A phenomenological theory of spherulitic crystallization. Journal of Applied Physics 8, 2409–2421. http://dx.doi.org/10.1063/1.1702757.

Keith, H.D., Padden, F.J., 1964. Spherulitic crystallization from the melt. I. Fractionation and impurity segregation and their influence on crystalline morphology. Journal of Applied Physics 35, 1270–1285. http://dx.doi.org/10.1063/1.1713606.

Kesler, S.E., Weiblen, P.W., 1968. Distribution of elements in a spherulitic andesite. American Mineralogist 53, 2025–2035.

Leveson, D.J., 1966. Geological Society of America Bulletin 77, 409–426. http://dx.doi.org/10.1130/0016-7606(1966)77 ([409:ORAR]2.0.CO;2).

Li, J., Dillon, S.J., Rohrer, G.S., 2009. Relative grain boundary area and energy distributions in nickel. Acta Materialia 57, 4304–4311. http://dx.doi.org/10.1016/j.actamat.2009.06.004.

Lindh, A., Näsström, H., 2006. Crystallization of orbicular rocks exemplified by the Slättemossa occurrence, southeastern Sweden. Geological Magazine 143, 713–722.

Lofgren, G., 1971a. Spherulitic textures in glassy and crystalline rocks. Journal of Geophysical Research 76, 5635–5648. http://dx.doi.org/10.1029/JB076i023p05635.

Lofgren, G., 1971b. Experimentally produced devitrification textures in natural rhyolitic glass. Geological Society of America Bulletin 82, 111–123. http://dx.doi.org/10.1130/0016-7606(1971)82[111:EPDTIN]2.0.C.

Lofgren, G., 1974. An experimental study of plagioclase crystal morphology: isothermal crystallization. American Journal of Science 274, 243–273. http://dx.doi.org/10.2475/ajs.274.3.243.

Lofgren, G., 1983. Effect of heterogeneous nucleation on basaltic textures: a dynamic crystallization study. Journal of Petrology 24, 229–255.

Magill, J.H., 2001. Spherulites: a personal perspective. Journal of Materials Science 36, 3143–3164.

Mainprice, D., Hielscher, R., Schaeben, H., 2011. Calculating anisotropic physical properties from texture data using the MTEX open-source package. In: Prior, D.J., Rutter, E.H., Tatham, D.J. (Eds.), Deformation Mechanisms, Rheology and Tectonics: Microstructures, Mechanics and Anisotropy. Geological Society, London, Special Publications 360, pp. 175–192.

Mainprice, D., Bachmann, F., Hielscher, R., Schaeben, H., 2014a. Descriptive tools for the analysis of texture projects with large datasets using MTEX — strength, symmetry, and components. In: Faulkner, D.R., Meckenburgh, J., Mariani, E. (Eds.), Rock Deformation from Field, Experiments and Theory: A Volume in Honour of Ernie Rutter. Geological Society, London, Special Publications 409. http://dx.doi.org/10.1144/SP409.8.

Mainprice, D., Bachmann, F., Hielscher, R., Schaeben, H., 2014b. Calculating anisotropic piezoelectric properties from texture data using the MTEX open source package. In: Faulkner, D.R., Meckenburgh, J., Mariani, E. (Eds.), Rock Deformation from Field, Experiments and Theory: A Volume in Honour of Ernie Rutter. Geological Society, London, Special Publications 409. http://dx.doi.org/10.1144/SP409.2.

Meyers, G.R., Mayo, S.C., Gureyev, T.E., Paganin, T.M., Wilkins, S.W., 2007. Polychromatic cone-beam phase-contrast tomography. Physical Review A 76, 045804.

Monecke, T., Renno, A.D., Herzig, P.M., 2004. Primary clinopyroxene spherulites in basaltic lavas from the Pacific Antarctic Ridge. Journal of Volcanology and Geothermal Research 130, 51–59.

Ort, H., 1992. Orbicular volcanic rocks of Cerro Panizos: their origin and implication for orb formation. Geological Society of America Bulletin 104, 1048–1058. http://dx.doi.org/10.1130/0016-7606(1992)104<1048:OVROCP>2.0.

Paganin, D., Mayo, S.C., Gureyev, T.E., Miller, P.R., Wilkins, S.W., 2002. Simultaneous phase and amplitude extraction from a single defocused image of a homogeneous object. Journal of Microscopy 206, 33–40. http://dx.doi.org/10.1046/j.1365-2818.2002.01010.x.

Pupier, E., Duchene, S., Toplis, M.J., 2007. Experimental quantification of plagioclase crystal size distribution during cooling of a basaltic liquid. Contributions to Mineralogy and Petrology 155, 555–570.

Seaman, S.J., 2013. Microtexture development during rapid cooling in three rhyolitic lava flows. American Mineralogist 98, 304–318. http://dx.doi.org/10.2138/am.2013.4313.

Shelley, D., 1993. Igneous and Metamorphic Rocks Under the Microscope—Classification, Textures, Microstructures and Mineral Preferred Orientations. Chapman & Hall, London, p. 445.

Smillie, R.O., Turnbull, R.E., 2014. Field and petrographical insight into the formation of orbicular granitoids from the Bonney Pluton, southern Victoria Land, Antarctica. Geological Magazine 151, 534–549.

Smith, J.V., Brown, W.L., 1988. Feldspar Minerals Volume 1 Crystal Structures, Physical, Chemical and Microtextural Properties. Springer-Verlag, Berlin, p. 828.

Smith, R.K., Tremallo, R.L., Lofgren, G.E., 2001. Growth of megaspherulites in a rhyolitic vitrophyre. American Mineralogist 86, 589–600.

Stasiuk, M.V., Barclay, J., Carroll, M.R., Jaupart, C., Ratte, J.C., Sparks, R.S.J., Tait, S.R., 1996. Degassing during magma ascent in the Mule Creek vent (U.S.A.). Bulletin of Volcanology 58, 117–130. http://dx.doi.org/10.1007/s004450050130.

Sutton, A.P., Balluffi, R.W., 1998. Interfaces in Crystalline Materials. Oxford University Press, Oxford, UK, p. 852.

Swanson, S.E., 1977. Relation of nucleation and crystal-growth rate to the development of granitic textures. American Mineralogist 62, 966–978.

Swanson, S.E., Naney, M.T., Westrich, H.R., Eichelberger, J.C., 1989. Crystallization history of Obsidian Dome, Inyo Domes, California. Bulletin of Volcanology 51, 161–176. http://dx.doi.org/10.1007/BF01067953.

Sylvester, A.G., 2011. The nature and polygenetic origin of orbicular granodiorite in the Lower Castle Creek pluton, northern Sierra Nevada batholith, California. Geosphere 7, 1–9. http://dx.doi.org/10.1130/GES00664.1.

Symes, R.F., Bevan, J.C., Qasim Jan, M., 1987. The nature and origin of orbicular rocks from near Deshai, Swat Kohistan, Pakistan. Mineralogical Magazine 51, 635–647.

Vernon, R.H., 1985. Possible role of superheated magma in the formation of orbicular granitoids. Geology 13, 843–845. http://dx.doi.org/10.1130/0091-7613(1985)13<843:PROSMI>2.0.CO;2.

Vetere, F., Iezzi, G., Behrens, H., Cavallo, A., Misiti, V., Dietrich, M., Knipping, J., Ventura, G., Mollo, S., 2013. Intrinsic solidification behaviour of basaltic to rhyolitic melts: a cooling rate experimental study. Chemical Geology 354, 233–242.

Voltolini, M., Zandomeneghi, D., Mancini, L., Polacci, M., 2011. Texture analysis of volcanic rock samples: quantitative study of crystals and vesicles shape preferred orientation from X-ray microtomography data. Journal of Volcanology and Geothermal Research 202, 83–95. http://dx.doi.org/10.1016/j.jvolgeores.2011.02.003.

Vona, A., Romano, C., 2013. The effects of undercooling and deformation rates on the crystallization kinetics of Stromboli and Etna basalts. Contributions to Mineralogy and Petrology 166, 491–509.

Vona, A., Romano, C., Dingwell, D.B., Giordano, D., 2011. The rheology of crystal-bearing basaltic magmas from Stromboli and Etna. Geochimica et Cosmochimica Acta 75, 3214–3236.

Watkins, J., Manga, M., Huber, C., Martin, M., 2009. Diffusion-controlled spherulite growth in obsidian inferred from H_2O concentration profiles. Contributions to Mineralogy and Petrology 157, 163–172. http://dx.doi.org/10.1007/s00410-008-0327-8.

X-TRACT, 2013. http://www.ts-imaging.net/.

Zandomeneghi, D., Voltolini, M., Mancini, L., Brun, F., Dreossi, D., Polacci, M., 2010. Quantitative analysis of X-ray microtomography images of geomaterials: application to volcanic rocks. Geosphere 6, 793–804.

Zucali, M., Voltolini, M., Ouladdiaf, B., Mancini, L., Chateigner, D., 2014. The 3D quantitative lattice and shape preferred orientation of a mylonitised metagranite from Monte Rosa (Western Alps): combining neutron diffraction texture analysis and synchrotron X-ray microtomography. Journal of Structural Geology 63, 91–105.